Shear thickening of dense suspensions: The role of friction

Sivadasan, V.; Lorenz, E.; Hoekstra, A.G.; Bonn, D.

DOI
10.1063/1.5121536
Publication date
2019
Document Version
Final published version
Published in
Physics of Fluids

Physics of Fluids ARTICLE scitation.org/journal/phf

Shear thickening of dense suspensions: The role of friction

Cite as: Phys. Fluids 31, 103103 (2019); doi: 10.1063/1.5121536
Submitted: 25 July 2019 • Accepted: 27 September 2019 •
Published Online: 16 October 2019

Vishnu Sivadasan,[1] Eric Lorenz,[1,2] Alfons G. Hoekstra,[1] and Daniel Bonn[3]

AFFILIATIONS

[1]Computational Science Lab, Institute for Informatics, University of Amsterdam, Amsterdam, The Netherlands
[2]Electric Ant Lab B.V., Amsterdam, The Netherlands
[3]Institute of Physics, Faculty of Science, University of Amsterdam, Amsterdam, The Netherlands

ABSTRACT

Shear thickening of particle suspensions is caused by a transition between lubricated and frictional contacts between the particles. Using three-dimensional (3D) numerical simulations, we study how the interparticle friction coefficient (μ_m) influences the effective macroscopic friction coefficient (μ) and hence the microstructure and rheology of dense shear thickening suspensions. We propose expressions for μ in terms of distance to jamming for varying shear stresses and μ_m values. We find μ to be rather insensitive to interparticle friction, which is perhaps surprising but agrees with recent theory and experiments. Unifying behaviors were observed between the average coordination numbers of particles across a wide range of viscous numbers and μ_m values.

I. INTRODUCTION

Understanding the rheological properties of shear thickening suspensions is scientifically challenging and highly relevant from the viewpoint of several applications.[1–4] The phenomenon of shear thickening[5–11] in which the viscosity increases with increasing shear rate and shear stress is attributed to the formation of frictional contacts between the particles as suggested by computational results[12–14] and confirmed by experiments.[15–19] Shear thickening suspensions can be characterized by their macroscopic friction coefficient μ, given by $\mu = \sigma_{\text{shear}}/P$, with σ_{shear} the shear stress and P the confining pressure. Using suspensions under constant confining pressure, Boyer *et al.*[11] demonstrated that μ is a unique function of a viscous parameter I_v defined as $I_v = \eta_f \dot{\gamma}/P$, where η_f and $\dot{\gamma}$ are the fluid viscosity and the shear rate, respectively. They observe similar $\mu(I_v)$ behavior for different materials (polystyrene, PMMA) and particle sizes. Gallier *et al.*[20] studied $\mu(I_v)$ rheology in simulations for $\phi < 0.45$ (ϕ being the particle volume fraction) and their simulations agree quantitatively with the experimental results. Recent studies by Chévremont *et al.*[21] and Trulsson *et al.*[22] have shed light upon the influence of the microscopic interparticle friction coefficient μ_m on μ, viscosity, and the jamming volume fraction. However, a more detailed analysis of μ and associated changes in the microstructure of the suspension is needed to further understand the behavior of the macroscopic friction coefficient μ and notably its relation with the microscopic friction coefficient μ_m. Here, we perform 3D numerical simulations of dense shear thickening suspensions with varying interparticle friction coefficients to study the associated changes on μ. Based on recent results on constitutive relationships for shear thickening systems,[23,24] we propose analytic expressions for μ in terms of the distance to jamming ($\phi_m - \phi$, where ϕ_m is the jamming volume fraction) for constant volume systems with varying pressure, shear stress, and μ_m values. Using the average coordination number as a parameter, the microstructure of the particles in the system is analyzed to assess its influence on μ. Finally, simulations of non-spherical particles are performed to study the effect of nonsphericity on the behavior of the macroscopic friction coefficient.

II. METHODS

The numerical simulations were performed using the simulation framework SuSi.[25] We use the Lattice Boltzmann Method (LBM) based fluid to simulate the fluid field and Lagrangian particles as the solid phase. The fluid-particle interactions are modeled with the Noble Torczynski Method.[26] Lubrication forces are calculated explicitly at particle gaps smaller than the LBM lattice spacing. Adaptive refinement of time steps is performed in order to ensure

numerical stability and accuracy, as the interparticle forces diverge at small particle gaps. The contact normal force $\mathbf{F}_{\text{rep}}$ between particles is calculated from the overlap of a contact repulsion layer[25] of specified thickness $d_c \approx 0.001R$,[12] where R is the mean radius of particles,

$$\mathbf{F}_{\text{rep}} = \begin{cases} -c_0 \dfrac{(d-d_c)^2}{d d_c^2}\mathbf{e}_h, & d \le d_c, \\ 0, & \text{otherwise}, \end{cases} \tag{1}$$

where c_0 is the repulsion coefficient, d is the gap between the particles, d_c is the repulsion layer thickness, and $\mathbf{e}_h$ is the connecting unit vector between the particles. The static and kinetic friction between particles is modeled as proposed by Luding.[27] Upon initiation of frictional contact between particle pairs, a linear spring of length ξ is initialized between the closest surface points to model static friction and is updated using the relative tangential velocity between the two contacting surface points. The maximum static friction is $F_s \le \mu_s|\mathbf{F}_{\text{norm,fric}}|$, as given by Coulomb's Law. The spring force $\mathbf{F}_{\text{spr}}$ is applied if the amplitude of $\mathbf{F}_{\text{spr}} = -k\boldsymbol{\xi}$ is smaller than the maximum possible static friction force F_s. Kinetic friction $F_k = \mu_k F_{\text{norm,fric}}$ is applied as a tangential force at the surface points if F_{spr} exceeds F_s. For kinetic friction, the static friction spring length is rescaled so that $F_{\text{spr}} = F_k$. In our simulations, we keep $\mu_s = \mu_k = \mu_m$, where μ_m is referred to as the microscopic friction coefficient.

The interacting particles are deemed frictional based on a critical load model,[12] where two particles are considered to be in friction if the normal force (F_{rep}) between the contacting particles exceeds a threshold value (F_{CL}). The static and kinetic friction is based on the normal force for friction ($F_{\text{norm,fric}}$), calculated as[12]

$$F_{\text{norm, fric}} = \begin{cases} |\mathbf{F}_{\text{rep}}| - F_{\text{CL}} & \text{if } |\mathbf{F}_{\text{rep}}| \ge F_{\text{CL}}, \\ 0 & \text{otherwise}. \end{cases} \tag{2}$$

For the simulations discussed in Sec. III, a 96 μm × 64 μm × 96 μm system is used, which contains ≈650 particles for $\phi = 0.56$. The particles have a mean diameter of 8 μm with a standard deviation of 0.4 μm to avoid crystallization. The particles are neutrally buoyant in the suspending fluid, which mimics water (fluid viscosity $\eta_f = 1.002 \times 10^{-3}$ Pa s, density $\rho_f = 1000$ kg/m^3). The simulated systems have a characteristic stress for frictional contacts, given by $\sigma_0 = F_{\text{CL}}/(6\pi R^2)$, where R is the average particle radius. $F_{\text{CL}} = 0.2$ nN in all simulations, and the tangential spring constant $k = 0.0361$ N/m. For the performed analysis, we choose instances of the system with the average shear stress greater than σ_0 so that frictional interactions are significant.

III. RESULTS AND DISCUSSION

A. Viscosity and normal stress differences

The viscosity of suspensions increases with the particle volume fraction and diverges when $\phi \to \phi_m(\mu_m)$ where ϕ_m is the jamming volume fraction associated with μ_m. Scalings such as the Maron-Pierce expression[28] $[\eta_r = (1-\phi/\phi_m)^{-2}]$ and the Krieger—Dougherty expression[29] $[\eta_r = (1-\phi/\phi_m)^{-2.5\phi_m}]$ have been used to describe the viscosity divergence with increasing ϕ. We compare our simulation results across various μ_m values against previous experiments,[11,30–32]

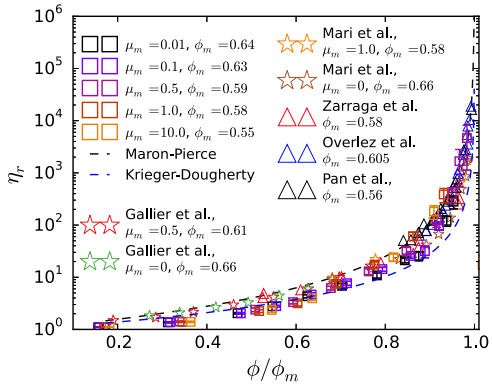

FIG. 1. Relative viscosity η_r vs particle volume fraction ϕ, normalized by the jamming volume fraction ϕ_m for our simulations (colored symbols), compared against: Maron-Pierce $[\eta_r = (1-\phi/\phi_m)^{-2}]$[28] scaling, Krieger and Dougherty[29] scaling $[\eta_r = (1-\phi/\phi_m)^{-2.5\phi_m}]$; simulation results by Gallier *et al.*[20] and Mari *et al.*;[12] experimental results from Overlez *et al.*,[31] Boyer *et al.*,[11] Zarraga *et al.*,[30] and Pan *et al.*[32] ϕ_m and μ_m (if available) are indicated for each source. Error bars shows the variation in viscosity. The simulation results correspond to the highest shear rate simulated for each individual ϕ and μ_m.

simulations,[12,20] and the aforementioned scalings[28,29] in Fig. 1. Our results are observed to be in agreement with the previous works. As expected, the viscosity of the system diverges close to ϕ_m and the value of ϕ_m increases with decreasing μ_m. We will explore this behavior further in Sec. III F.

Shear thickening is also associated with the presence of normal stress differences.[5,32] The second normal stress difference N_2 ($N_2 = \sigma_{22} - \sigma_{33}$, where σ_{22} and σ_{33} are the normal stresses in the shear gradient and vorticity directions) has consistently been found to be negative in experiments[30,33–36] and simulations[20,37,38] alike, and its magnitude increases linearly with shear stress σ_{shear}. A fit of $N_2/\sigma_{\text{shear}} = -4.4\phi^3$ was suggested by Dai *et al.*[33] for the variation of N_2 with ϕ. We show the comparisons between our results, the previous experiments, and simulations in Fig. 2(a). Our simulation results again show good agreement with the results from the literature.

The first normal stress difference N_1 ($N_1 = \sigma_{11} - \sigma_{22}$, σ_{11} is the normal stress in the shear direction) has been a topic of debate since there are considerable differences in the available experimental data.[33,34,36] N_1 is generally smaller in magnitude compared to N_2. The behavior of N_1 is less well understood since even the algebraic sign of N_1 appears to depend on experimental conditions.[32] We compare N_1 observed in our simulations against the existing literature in Fig. 2(b). N_1 obtained in our simulations closely resembles the works by Royer *et al.*[18] who observed a negative to positive transition for N_1 with increasing ϕ. Recent studies[39] have made advances to address some of the outstanding questions about N_1.

B. Viscous number rheology

The macroscopic friction coefficient (μ) of suspensions is characterized by the viscous number (I_v) of the suspension flow. I_v is defined as

$$I_v = \eta_f \dot{\gamma}/P, \tag{3}$$

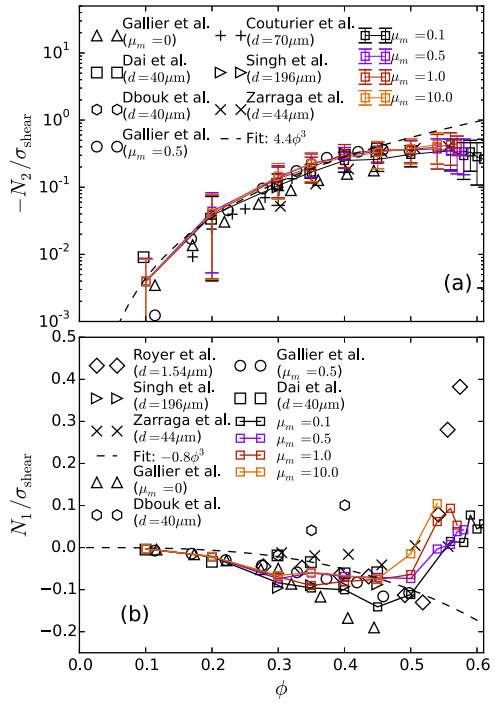

FIG. 2. Ratio of the normal stress difference to the shear stress (a) $-N_2/\sigma_{shear}$ and (b) N_1/σ_{shear} as a function of ϕ for various μ_m values. Simulations (colored symbols) are compared against: experimental results of Dai *et al.*,[33] Dbouk *et al.*,[36] Couturier *et al.*,[35] Zarraga *et al.*,[30] Singh and Nott,[34] and Royer *et al.*;[18] simulation results of Gallier *et al.*[20] and the fits suggested by Dai *et al.*[33] Relevant information about the particle diameter d and μ_m are shown in the legends. Results from simulations are taken over a range of $\sigma_{shear}/\sigma_0 \in [0.01, 100]$. The values of N_1 have significant fluctuations, and the averaged values are presented.

where η_f is the fluid viscosity, $\dot{\gamma}$ is the shear rate, and P is the pressure in the system. The viscous number can be seen as the ratio of the internal time scale of microscopic particle rearrangements in a viscous system (η_f/P), to the macroscopic flow time scale ($1/\dot{\gamma}$). Boyer *et al.*[11] used pressure imposed flows to study variation in μ with I_v, where systems of hard spheres were sheared at constant pressure (P) and shear rate ($\dot{\gamma}$) while the system was allowed to dilate (changing ϕ) in order to keep P constant. They demonstrated that μ of suspensions is the sum of contact (μ_c) and hydrodynamic (μ_h) stress contributions, as shown in the following:

$$\mu(I_v) = \underbrace{\mu_1 + \frac{\mu_2 - \mu_1}{1 + I_0/I_v}}_{\mu_c} + \underbrace{I_v + \frac{5}{2}\phi_m I_v^{\frac{1}{2}}}_{\mu_h}, \tag{4}$$

where, μ_1 is the limit of the particle contact contribution to the macroscopic friction (μ_c) at vanishing viscous numbers, and μ_2 is the maximum μ_c at $I_v \to \infty$ as observed in granular flows.[40,41] I_0 represents the scale over which $\mu_c(I_v)$ changes and is observed to be constant for a given particle shape. ϕ_m is the jamming volume fraction. $\mu_h(I_v)$ is designed to reproduce the Einstein viscosity at low ϕ and be nonsaturating at high I_v. Here, simulations of constant ϕ and $\dot{\gamma}$ with varying P are performed to study $\mu(I_v)$. In this study, we define P as the average of the diagonal elements of the stress tensor in the system, i.e., $P = \sum_{i=1}^{3} \sigma_{ii}/3$. We systematically vary the microscopic friction coefficient μ_m and compare to the predictions of $\mu(I_v)$ rheology [Eq. (4)] to see if the constant ϕ and $\dot{\gamma}$ simulations conform to the predictions of $\mu(I_v)$ rheology.

Figure 3(a) compares the results from our simulations to the $\mu(I_v)$ rheology predicted by Eq. (4), and the experimental results from Boyer *et al.*[11] Suspensions of different ϕ values were simulated to obtain the range of I_v values. It can be observed that $\mu \approx 0.34$ at vanishing I_v, which is similar to the values obtained in experiments.[11,40] Using $\mu_2 = 0.7$ and $I_0 \approx 0.009$ provides a good fit to the simulation data. The value for μ_2 is the same as that observed previously in experiments and simulations of spherical particles.[11,20]

At vanishing I_v, we find high corresponding ϕ values similar to that in experiments.[11] Under constant ϕ settings, the range of I_v values accessible for each ϕ value is limited [as seen in Fig. 3(b)], and multiple simulations of varying ϕ values are required to capture I_v values varying in orders of magnitude. This issue can be overcome by allowing the system to dilate in order to change ϕ, as done in

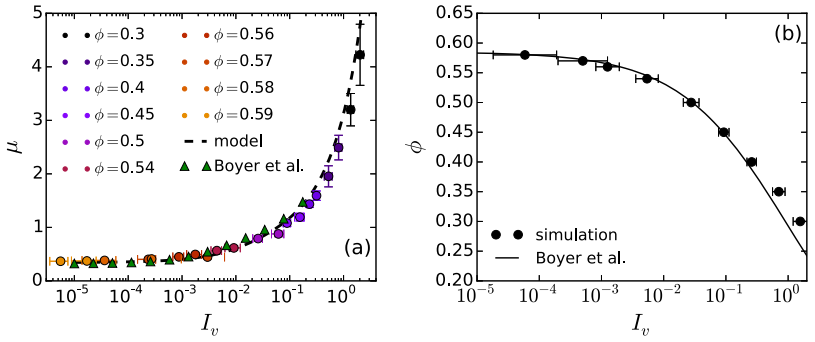

FIG. 3. (a) Macroscopic friction coefficient μ vs viscous number I_v comparison between simulation and the model. Dots represents μ prediction from simulations of ϕ corresponding to its color. The dashed line shows the $\mu(I_v)$ prediction from Eq. (4) with $\mu_1 = 0.34$ (minimum μ observed), $\mu_2 = 0.7$, and $I_0 = 0.009$ providing a good fit to the simulation results. The microscopic friction coefficient $\mu_m = 0.5$. Triangles represent the experimental results from Boyer *et al.*[11] Vertical and horizontal error bars correspond to variation in μ and I_v in the data, in each I_v interval. (b) Variation in ϕ vs viscous number I_v. Dots represent simulation results, and the line represents results from Boyer *et al.*[11] Error bars represent the range of I_v values observed for a given ϕ.

experiments. The variation in ϕ with I_v is shown in Fig. 3(b), along with the experimental observation from Boyer *et al.*[11] The simulations show good agreement with the previous experimental results and the theoretical scalings.

C. Viscosity variation and effect on macroscopic friction

Viscosity and macroscopic friction coefficient are inherently related. Simple algebraic manipulation of Eq. (3) shows that μ and I_v are linked to the relative viscosity η_r as [see Eq. (5), from Boyer *et al.*[11]]

$$\eta_r = \frac{\mu}{I_v}. \tag{5}$$

Figure 4(a) shows the relative viscosity η_r ($\eta_r = \eta/\eta_f$, η being the suspension viscosity) as a function of the shear rate in our simulations (same system as in Fig. 3) for various particle volume fractions. With increasing ϕ and $\dot{\gamma}$, an increased relative viscosity η_r is observed in the system. At lower ϕ values ($\phi < 0.56$), we see CST and subsequently DST at higher ϕ values. The macroscopic friction coefficient μ also shows variation with ϕ and $\dot{\gamma}$, as shown in Fig. 4(b). With increasing ϕ, pronounced reduction in μ is observed, and when the system undergoes shear thickening, we find μ to reduce again. Similar observations were made in two dimensional systems by Thomas *et al.*[42] This happens as a result of the difference in scaling of the pressure compared to σ_{shear} during shear thickening. Viewed from the perspective of viscous number rheology, this is a result of the reduction in I_v during shear thickening as a result of the pressure increasing at a faster rate compared to the increase in $\dot{\gamma}$ [see Eq. (3)]. This can also be interpreted in terms of distance to jamming, as shown in Sec. III F. As shown in Sec. III F, the closer a system is to jamming (in terms of say, $\phi_m - \phi$), the lower the value of μ. With increasing ϕ, the value of $\phi_m - \phi$ reduces and the system moves closer to jamming. Consequently, a reduction in μ is observed. When the system undergoes shear thickening, ϕ_m decreases as more particles become frictional [see Eq. (9)] and as a result, $\phi_m - \phi$ reduces further; the system again moves closer to jamming and μ is reduced again. Next, we compare the variation in η_r with μ in Fig. 4(c). As viscosity increases, we see reduced μ values. As ϕ approaches $\phi_m \approx 0.59$, μ approaches μ_1 and η_r diverges. The collapse of the data onto the same curve might be surprising but can be rationalized. As shown in Eq. (5), η_r is related to μ and I_v. Since μ is a function of I_v described by Eq. (4), η_r is simply a function of I_v. By substituting Eq. (4) in Eq. (5), we can describe this relationship quite well, as shown in Fig. 4(c). In Fig. 4(d), we analyze the frictional ($\sigma_{shear} > \sigma_0$) and nonfrictional ($\sigma_{shear} < \sigma_0$) states of the same system separately. We see that $\eta_r(\mu)$ follows slightly different curves for frictional and frictionless states in comparison, as frictionless states effectively have a microscopic friction coefficient $\mu_m = 0$. Thus, $\eta_r(\mu)$ would diverge at a lower μ_1 (see the Sec. III E), but since we do not simulate ϕ values close to the ϕ_m value associated with $\mu_m = 0$ ($\phi_m^{\mu_m=0} \approx 0.64$), the divergence for the nonfrictional states is not approached.

D. Effect of varying the critical load for friction

Varying the value of the critical load F_{CL} changes the onset force for friction between contacting particles. Consequently, the characteristic stress σ_0 for friction and shear thickening depends on F_{CL}, as $\sigma_0 \propto F_{CL}/R^2$. We present the results of varying F_{CL} over three orders of magnitude in Fig. 5. Changing F_{CL} does not change the results of $\mu(I_v)$ in viscous number rheology in our constant ϕ systems. The viscous number is given by $I_v = \eta_f \dot{\gamma}/P$ and the macroscopic friction coefficient $\mu = \sigma_{shear}/P$. These quantities change depending on the scaling of σ_{shear}, P and $\dot{\gamma}$ with respect to each other. Prior to or postshear thickening, the scaling of P and σ_{shear} with $\dot{\gamma}$ does not change, as evidenced by the constant viscosity in these states. Thus, $\mu(I_v)$, which depends on the ratio of these terms does not change prior or post shear thickening. During shear thickening, the scaling of P, σ_{shear}, and $\dot{\gamma}$ changes with respect to each other due to the additional force scaling (compared to the nonfrictional state) due to the progressive increase in the fraction of frictional contacts.[43] As a result, variation in μ and I_v are observed only during shear thickening. This can be readily observed in Fig. 4(b) where the μ varies during shear thickening and remains constant prior to and postshear thickening.

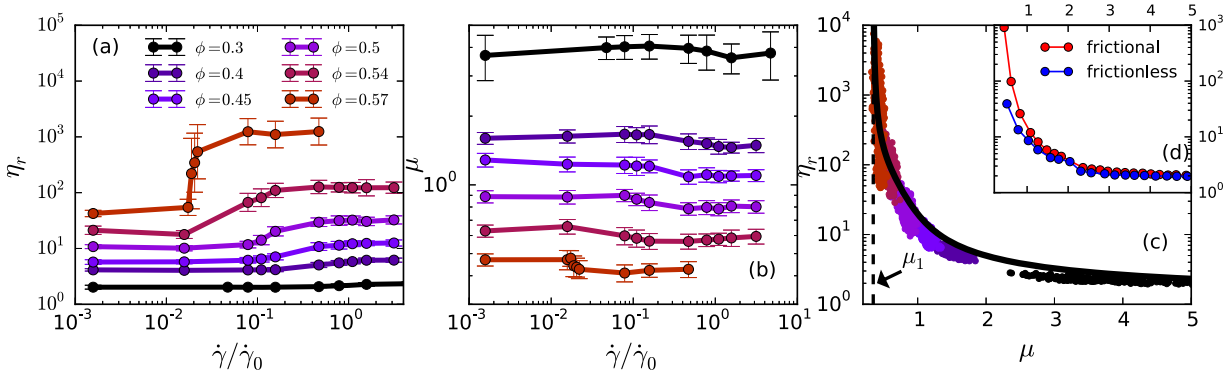

FIG. 4. Relative viscosity η_r and macroscopic friction coefficient μ variation during shear thickening, for $\mu_m = 0.5$. (a) Relative viscosity η_r vs shear rate $\dot{\gamma}$. Shear rate $\dot{\gamma}$ is normalized by $\dot{\gamma}_0 = \sigma_0/\eta_f$. (b) μ vs normalized $\dot{\gamma}$. (c) η_r variation with μ. $\mu_1 = 0.34$ is indicated by the dashed vertical line. Black line represents predictions from Eqs. (4) and (5), with parameters the same as that in Fig. 3. Colors represent the same ϕ values in (a, b, c). States of the system where $\sigma_{shear} > \sigma_0$ are chosen in order to avoid nonfrictional states. (d) η_r, μ for frictional ($\sigma_{shear} > \sigma_0$) and frictionless ($\sigma_{shear} > \sigma_0$) states analyzed separately (note the difference in the divergences).

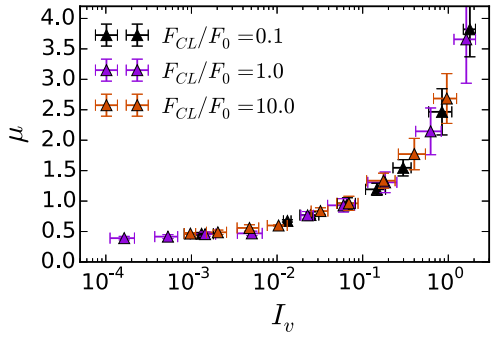

FIG. 5. Effect of the variation in F_{CL} on $\mu(I_v)$. F_0 = 2 nN, μ_m = 0.5, and measurements over $\sigma_{shear}/\sigma_0 \in [0.01, 100]$.

E. Effect of varying microscopic friction coefficient

The properties of the particle contacts have significant influence on the rheology of suspensions. Purposeful roughening of particles has shown to increase the viscosity of suspensions in the works of Moon *et al.*[44] and Lootens *et al.*[45] Hsu *et al.*[46] and Lootens *et al.*[45] also found the jamming transition to happen at lower volume fractions upon using rougher particles, as rougher particles have higher microscopic friction coefficients.

The microscopic friction coefficient μ_m has a significant impact on the shear thickening process. Experimental results from Lootens *et al.*,[45] simulations by Mari *et al.*,[12] and theoretical models by Singh *et al.*[23] show that with decreasing μ_m, the strength of shear thickening reduces in dense suspensions and at $\mu_m = 0$, shear thickening disappears altogether. In order to study the effect of changing μ_m on μ, we perform simulations of $0.01 \le \mu_m \le 10$, while keeping all other system parameters the same. This amounts to over 500 individual simulations. In agreement with the literature, we find the microscopic friction coefficient to affect the viscosity significantly, as shown in Fig. 6(a). With lower μ_m values, shear thickening observed becomes progressively less pronounced.

Earlier simulation studies of the role of the microscopic friction coefficient (μ_m) in viscous number rheology were performed at large viscous numbers ($I_v > 0.1$) with limited overlap between I_v ranges studied in experiments.[20] Here, a larger range of I_v values is accessed, allowing comparisons with experimental results at lower I_v values, as shown in Fig. 3. In the previous works of Gallier *et al.*,[20] it was postulated that the master curve for $\phi(I_v)$ observed by Boyer *et al.* [Fig. 2(d) in Ref. 11] was possibly not unique across various friction coefficients, as the microscopic friction coefficients in their experiments may not have been varied significantly. Since we are able to access the low I_v regime, we find evidence that this is indeed true, as shown in Fig. 6(b). With varying μ_m, we find different curves of $\phi(I_v)$, each saturating at low I_v at different ϕ_m values corresponding to the μ_m used. Upon normalizing ϕ values with ϕ_m, we see in Fig. 6(c) that the results obey Eq. (11) as suggested by Boyer *et al.*,[11] and that this relationship is insensitive to μ_m. This was also reported by Trulsson *et al.*[22] in their 2D simulations and recently observed by Chévremont *et al.*[21] in their 3D simulations. It should be noted that the works of Chévremont *et al.* and Trulsson *et al.* have constant pressure with varying ϕ, while our system has constant ϕ with varying pressure.

We now look at the influence μ_m has on the $\mu(I_v)$ relationships. In Fig. 7(a), the simulation results of $\mu(I_v)$ for various μ_m values are shown. At large I_v values ($I_v > 0.1$), $\mu(I_v)$ is similar for all μ_m values. At vanishing I_v values ($I_v < 10^{-4}$), the minimum $\mu(I_v)$ (i.e., μ_1) reduces with decreasing μ_m, as shown in Fig. 7(c). This observation is in agreement to that made in past simulations of 2D granular and suspension flows.[22,47] Interestingly, the relationship between $\mu - \mu_1$ and I_v collapses to the same curve for all μ_m values in this system [see Fig. 7(b)]. Such a collapse was not observed when spherical particle suspensions studied in this section are compared against nonspherical particle suspensions (see Sec. III H), suggesting that particle shape is a factor here. The change in μ_1 with μ_m follows a sigmoidal relationship, as observed in Fig. 7(c). The collapse of $\mu - \mu_1$ for $I_v < 10^{-3}$ with the viscous number is obviously due to μ being constant and equal to μ_1 in this range. Within the intermediate viscous number range ($10^{-3} \le I_v \le 10^{-1}$) where the particle contact contribution [μ_c in Eq. (4)] to μ remains dominant, the variation in μ with the microscopic friction coefficient μ_m is dictated by the variation in $\mu_2 - \mu_1$ with μ_m. Seeing that μ_2 is rather insensitive to microscopic interparticle friction coefficients (μ_2 varies between 0.7 and 0.8 for completely frictionless and frictional particles,

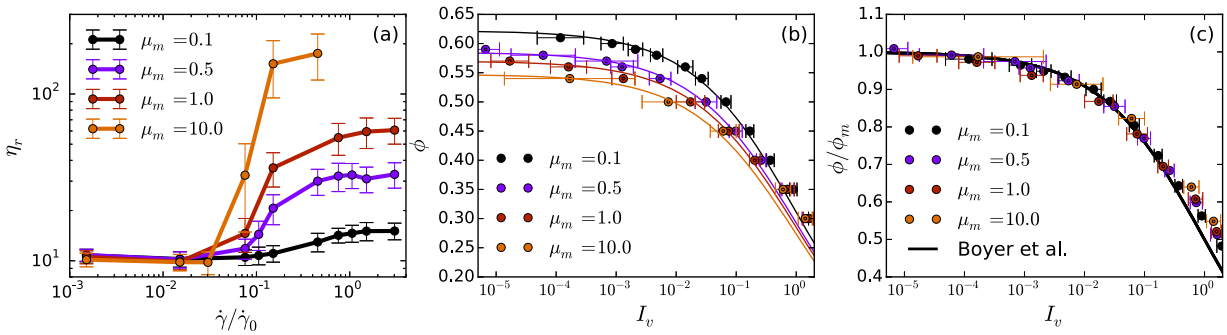

FIG. 6. (a) Relative viscosity η_r vs shear rate $\dot{\gamma}$ for ϕ = 0.5 under different microscopic friction coefficients μ_m. (b) Variation of I_v with various ϕ values. Dots represent the simulation results, and error bars represent the range of I_v observed at the corresponding ϕ. Lines represent the prediction from Eq. (11) with ϕ_m taken from simulation results at low I_v. (c) ϕ/ϕ_m as a function of I_v for various μ_m values. Solid line represent Eq. (11) suggested by Boyer *et al.*[11] Results compiled over $\sigma_{shear} > \sigma_0$.

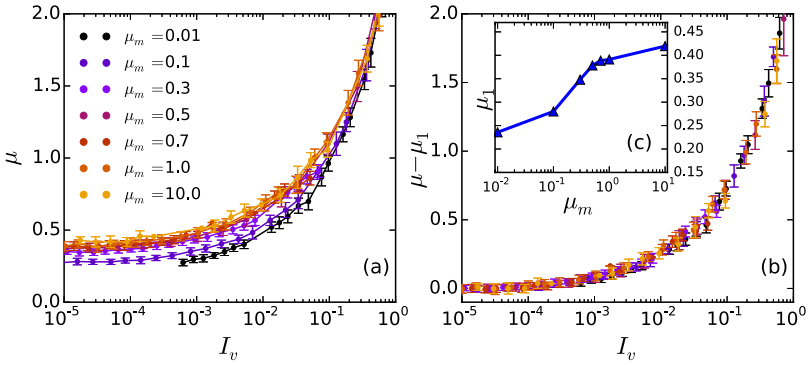

FIG. 7. (a) Macroscopic friction coefficient μ vs viscous number I_v for different microscopic friction coefficients (μ_m). Each dot represents the prediction from simulations of corresponding μ_m value. Results are compiled over various ϕ and $\dot{\gamma}$ values for each μ_m value in consideration. (b) $\mu - \mu_1$ vs I_v where μ_1 is the minimum μ observed. (c) Change in the minimum μ observed (i.e., μ_1) with μ_m.

respectively[20]), we estimate that the largest difference in $\mu - \mu_1$ between systems of $\mu_m = 0.01$ and $\mu_m = 10.0$ should be ≈0.2, which agrees with the observed variations in $\mu - \mu_1$ with μ_m at $I_v \approx 10^{-1}$. For large viscous number range ($I_v > 10^{-1}$), the variations in μ are dominated by the hydrodynamic component [μ_h in Eq. (4)], and does not depend on the friction.

The observation that $(\mu - \mu_1)$ as a function of I_v collapses onto the same curve for $0.01 \leq \mu_m \leq 10$, and $(\mu - \mu_1) \to 0$ the closer the system is to jamming, suggests that $\mu - \mu 1$ could be considered as a measure of the distance to jamming for these systems. In other words, the value of $\mu - \mu_1$ is dictated by the "closeness" of a system to jamming. At the same microscopic to macroscopic particle rearrangement time scale ratios (i.e., I_v), all systems have the same distance to jamming, regardless of their microscopic friction coefficient. This also entails that if $\mu - \mu_1$ indeed is a measure of the distance of a system from jamming, it should have a mapping to some other measure of distance to jamming, such as $\phi_m - \phi$. We shall explore this in Sec. III F.

F. Macroscopic friction coefficient and distance to jamming

In the simulations, a range of shear stresses (σ_{shear}), volume fractions (ϕ) and microscopic friction coefficients (μ_m) are studied. From previous experiments and simulations,[23,24] we understand the effect of changing each of these parameters on the rheology, especially on the jamming volume fraction (ϕ_m). Shear thickening is due to the formation of system spanning frictional networks, and the best way to describe this is to look at the fraction of frictional particles in the system. Beyond a characteristic shear stress σ_0, the fraction of particles in the system that have frictional contacts (f) increases until all particles become frictional.[12] This increase in f with shear stress σ_{shear} can be described[48] as

$$\sigma_0 = F_{\text{CL}}/6\pi R^2, \tag{6}$$

$$\tilde{\sigma} = \sigma_{\text{shear}}/\sigma_0, \tag{7}$$

$$f = e^{(-1.45/\tilde{\sigma})}, \tag{8}$$

where R is the average radius of the particles, F_{CL} is the onset normal force between particles to initiate friction, and $\sigma_0 = F_{\text{CL}}/(6\pi R^2)$ is the characteristic stress for the onset of friction. Increasing the fraction of frictional particles leads to a lower jamming volume fraction ϕ_m, as ϕ_m for frictional particles is lower than nonfrictional particles.[23,24] This is a result of the frictional particles requiring a smaller number of interparticle contacts to be arrested in comparison with frictionless particles.[49] The average coordination number for jamming (Z_J) in suspensions varies continuously between $Z_J(\mu_m = \infty) = 4$ and $Z_J(\mu_m = 0) = 6$ in suspensions. Increasing the fraction of frictional particles in the system reduces the jamming volume fraction ϕ_m from that of a lubricated, nonfrictional suspension (ϕ_J^0) to that of a frictional suspension (ϕ_J). $\phi_J(\mu_m)$ is the jamming volume fraction in a suspension with all particles in frictional contact and is a decreasing function of the microscopic friction coefficient μ_m. Hence, the volume fraction associated with jamming varies with μ_m and the fraction of frictional particles f in the system, and can be described[23] by

$$\phi_m(\tilde{\sigma}, \mu_m) = \phi_J(\mu_m) f(\tilde{\sigma}) + \phi_J^0(1 - f(\tilde{\sigma})), \tag{9}$$

where $\phi_J(\mu_m)$ represents the jamming volume fraction when $f = 1$ for a given microscopic friction coefficient μ_m. ϕ_J^0 is the jamming volume fraction when $f = 0$, which is equivalent to a $\mu_m = 0$ (frictionless) state. Changing the microscopic friction coefficient μ_m influences ϕ_m, as lowering μ_m increases[23] ϕ_J, according to Eq. (10),

$$\phi_J(\mu_m) = \phi_J^0 - (\phi_J^0 - \phi_J^\infty) e^{-\mu_\phi/\mu_m}. \tag{10}$$

Here, ϕ_J^∞ is the jamming volume fraction at large μ_m values, and μ_ϕ is a constant. Boyer *et al.*[11] proposed a model for I_v in terms of ϕ_m and ϕ as

$$\phi(I_v) = \frac{\phi_m}{1 + I_v^{0.5}}, \tag{11}$$

and when substituted in Eq. (4), this gives μ as a function of ϕ_m and ϕ,

$$\mu(\phi, \phi_m) = \underbrace{\mu_1 + \frac{\mu_2 - \mu_1}{1 + I_0\phi^2/(\phi_m - \phi)^2}}_{\mu_c} + \underbrace{\left(\frac{\phi_m - \phi}{\phi}\right)^2 + \frac{5}{2}\frac{\phi_m}{\phi}(\phi_m - \phi)}_{\mu_h}. \tag{12}$$

Under constant volume settings, the fraction of the frictional contacts varies with shear stress (or shear rate) in the system, which

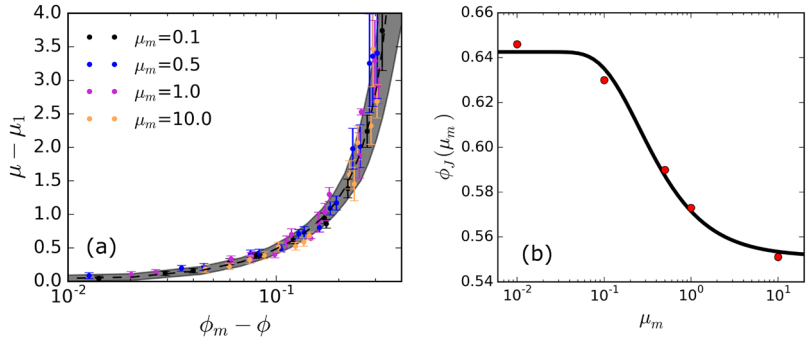

FIG. 8. (a) Macroscopic friction coefficient $\mu(\phi, \sigma_{\text{shear}}, \mu_m) - \mu_1(\mu_m)$ vs distance to jamming $\phi_m - \phi$ for different μ_m, σ_{shear}, and ϕ values. The shaded area represents the range of values of $\mu - \mu_1$ predicted by Eq. (12), correcting for changes in ϕ_m according to Eqs. (6)–(10), and the dashed line represents their mean. μ_1 values are as given by Fig. 7(b), $\mu_2 = 0.7$. (b) Frictional jamming volume fraction $\phi_J(\mu_m)$ for different microscopic friction coefficient (μ_m) values. Red dots represent the simulation data, while the curve represents the model presented in Eq. (10) with $\phi_J^0 = 0.643$, $\phi_J^\infty = 0.55$, and $\mu^\phi = 0.25$.

in turn varies ϕ_m. We can account for this variation in ϕ_m by employing Eqs. (6)–(10). This helps to predict ϕ_m in our constant volume system in terms of σ_{shear} and μ_m which in turn enables an analysis of μ as a function of $\phi_m - \phi$ (i.e., a distance to jamming metric) and compare against the predictions from Eq. (12).

Figure 8(a) shows the $\mu - \mu_1$ as a function of $\phi_m - \phi$ compiled over a range of σ_{shear}, ϕ, and μ values. The simulation results show agreement with the predictions from theory outlined in Eqs. (6)–(12). The changes in ϕ_J with μ_m are taken into account by using their relationship outlined in Eq. (10), as shown in Fig. 8(b). The simulation results agree with the theoretical assumption that, by accounting for changes in ϕ_m with σ_{shear} and μ_m, the values of μ across different σ_{shear} and μ_m values collapse to the regime outlined in Fig. 8(a). The change in the frictional jamming volume fraction ϕ_J with μ_m is shown in Fig. 8(b), along with the model presented in Eq. (10). The results also show that $\mu - \mu_1$ is indeed a measure for the distance to jamming, as suggested in Sec. III E.

G. Microstructure changes

The microscopic friction coefficient plays an important role in the nature of contact networks formed at jamming. The mean coordination number at which the suspension jams (Z_J) is inversely dependent on μ_m, as $Z_J(\mu_m = 0) = 6$ and $Z_J(\mu_m = \infty) = 4$.[49] The evolution of μ with the average coordination number (Z) under varying μ_m values, thus, is of interest. It is also compelling to view $\mu(I_v)$ rheology in terms of the evolution of Z.

Figure 9(a) shows average coordination number $Z(I_v)$ under various μ_m values. Z is calculated per particle by counting the number contacts it makes, i.e., cases where $r_{ij} - R_i - R_j \le d_c$, where $r_{i,j}$ are the distance between the particles and $R_{i,j}$ are their radii. Even though the data is compiled from various ϕ and σ_{shear} values, $Z(I_v, \mu_m)$ collapses to unique curves depending on μ_m. The maximum coordination number is $Z \approx 4$ at $\mu_m = 10.0$ and saturates at higher maximum values (Z_J) with reducing μ_m as expected from $Z_J(\mu_m)$ relationship described before. The low Z values at large I_v sheds light on the insensitivity of $\mu(I_v)$ rheology to changes in μ_m in these I_v ranges. $\mu(I_v)$ rheology hence is essentially the process of varying coordination numbers between zero and $Z_J(\mu_m)$. Upon normalizing Z by $Z_J(\mu_m)$, the different $Z(\mu_m)$ curves collapse to a single curve, which can be modeled as

$$\frac{Z}{Z_J} = 1 - \left(1 + I_v^{\alpha_1}\right)^{-\beta_1}, \tag{13}$$

where $\alpha_1 = 0.77$ and $\beta_1 = 0.3$. The variation in Z_J between 6 and 4 depending on μ_m can also be modeled using the expression

$$Z_J = 6 - 2\left(1 + \mu_m^{\alpha_2}\right)^{-\beta_2}, \tag{14}$$

where $\alpha_2 = -1.72$ and $\beta_2 = 0.27$. Figure 9(b) shows Z/Z_J as a function of I_v, and it can be observed that the data collapses to a single curve, modeled by Eq. (13). The variation in Z_J with μ_m, modeled by Eq. (14) is shown in Fig. 9(c). It is relevant to note that the variation

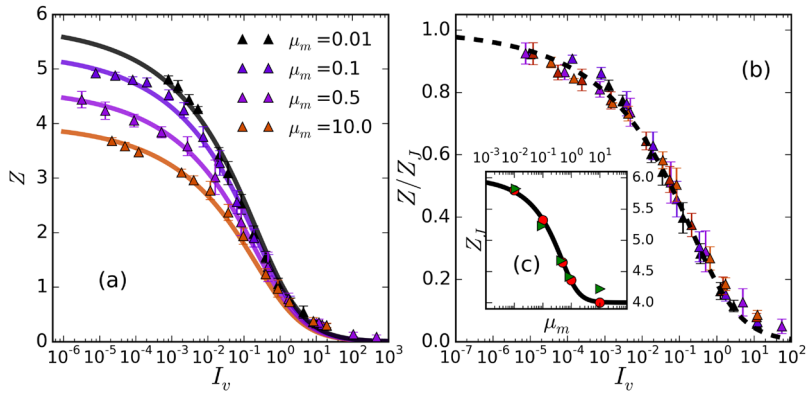

FIG. 9. (a) Average coordination number Z as a function of viscous number I_v for different μ_m compiled across different ϕ and σ_{shear} values. Each dot corresponds to simulation results at corresponding μ_m. Lines show the prediction of $Z(I_v)$ from Eqs. (13) and (14). (b) Z normalized by jamming coordination number Z_J vs I_v. The dashed line represents the $Z/Z_J(I_v)$ model from Eq. (13) while dots represent the simulation results of μ_m. (c) Variation in Z_j with μ_m. The dots show Z_J as observed in simulations at vanishing I_v. The line represents the $Z_J(\mu_m)$ model from Eq. (14). Green triangles represent the random loose packing limits in simulations of the granular system.[49]

in Z_J with μ_m is found to be quite similar to the change in the coordination numbers associated with minimum random loose packing (RLP) limit observed in dry granular systems.[49] The minimum RLP coordination number corresponds to the minimum coordination number required to obtain a disordered, mechanically stable jammed system. As the limits of jamming are prescribed entirely by the properties of the particles, it is conceivable that the characteristics related to jamming in granular systems devoid of fluid is to be expected in suspensions as well.

The effect of changing Z on μ, under various μ_m values is shown in Fig. 10(a). $\mu(Z)$ values reasonably collapses into a single curve for all values of μ_m studied. This demonstrates that the minimum μ achieved at low I_v values (i.e., μ_1) is determined by Z_J. As Z_J is inversely related to μ_m, the relationship between μ_1 and μ_m depicted in Fig. 7(b) can be rationalized. Assuming a range of I_v values, one can calculate and compare μ against Z for a given μ_m value using the relationships outlined in Eqs. (4), (10), (13), and (14). As shown in Fig. 10(a), the theoretical predictions of $\mu(Z, \mu_m = 0.5)$ is in agreement with the simulation results. Consequently, the variation in μ with ϕ also collapses reasonably onto a simple curve across the various μ_m values studied, as seen in Fig. 10(b). This behavior is observed in 2D simulations of sheared suspensions and dense granular systems[42,47] and experimentally by Boyer *et al.*[11] With increasing volume fraction, under a given shear rate, the shear stress and normal stresses become larger, but their ratio (μ) reduces till $\mu = \mu_1$ at jamming [see Figs. 10(d)–10(f)].

This implies that the jamming volume fraction determines μ_1, the minimum macroscopic friction coefficient. The lower the jamming volume fraction, the higher the observed μ_1; see Fig. 10(c). Our simulations of nonspherical particle suspensions (see Sec. III H) that jam at a lower volume fraction compared to spherical particles also agree with this observation, as shown in Fig. 10(c).

H. Nonspherical particles

Particle shapes have significant effects on the shear thickening behavior of the suspensions. Cornstarch particles are observed to shear thicken at much lower ϕ_m values ($\phi_m \approx 0.44$)[6] in comparison to suspensions of spherical particles which shear thicken around $\phi_m = 0.56$. Simulation results[25] show that frictional jamming volume fraction ϕ_J^∞ is lowered when particles shapes become "cornstarch-like." In the interest of comparing the macroscopic friction coefficient variation in spherical particles to that of nonspherical particles, simulations of "cornstarch-like" nonspherical particle suspensions were performed. The "cornstarch-like" particles were created using overlapping spheres of varying sizes, as outlined in Ref. 25. The nonspherical particles are bimodal with diameters of 8 μm (50% by volume) and 11.2 μm (50% by volume) and a standard deviation about $0.01R$, calculated based on the largest chord length. The particles have an aspect ratio distribution with a mean of 1.1 and standard deviation of 0.1. A representation of the nonspherical particles used is provided in Fig. 11(a)(inset).

Figure 11(a) compares $\mu(I_v)$ for spherical particle suspensions and nonspherical particle suspensions. At high viscous numbers, $\mu(I_v)$ for spherical and nonspherical particle suspensions tends to be the same. This is understandable, as at high I_v values the coordination numbers of the particles (spherical or nonspherical) in the suspensions reduces and particle shapes become increasingly less relevant. However, at small I_v values, $\mu(I_v)$ behavior of nonspherical particle suspensions deviates from that of spherical particle

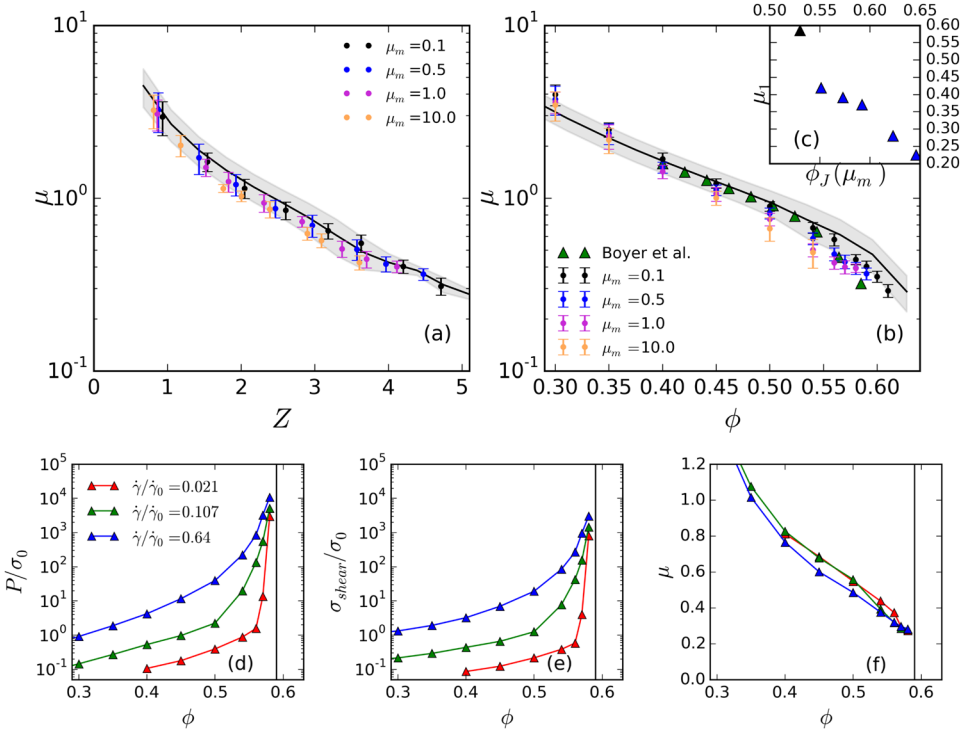

FIG. 10. (a) Variation in the macroscopic friction coefficient μ with average coordination number Z compiled across different μ_m and ϕ values. The solid line and shaded area represent the mean and range of values $\mu(Z)$ under various μ_m values predicted by Eqs. (4), (13), and (14). (b) Variation of μ with ϕ for various μ_m values. The solid line and shaded area represent the predicted range of $\mu(\phi)$ for various μ_m values by Eqs. (9)–(12). Green triangles represent the experimental results from Boyer *et al.*[11] (c) Minimum macroscopic friction coefficient (μ_1) achieved at jamming as a function of the jamming volume fraction $\phi_J(\mu_m)$. Black triangle represents the μ_1 observed at jamming for suspensions of nonspherical particles discussed in Sec. III H. [(d) and (e)] Pressure P and shear stress σ_{shear} normalized by σ_0 scaling with volume fraction for various shear rates for μ_m = 0.5. (f) Macroscopic friction coefficient μ measured for the pressure and shear stresses shown in [(d) and (e)]. Vertical black lines show the jamming volume fraction.

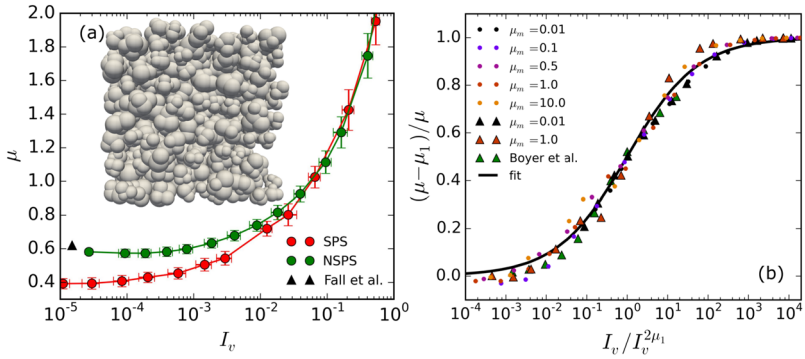

FIG. 11. (a) Macroscopic friction coefficient μ vs viscous number I_v for spherical particle suspensions (SPS) and nonspherical particle suspensions (NSPS) with μ_m = 1.0. Black triangle represent the macroscopic friction coefficient measured close to jamming in experiments with cornstarch suspensions.[6] **(inset)**: Representation of the nonspherical particles used in the simulations. (b)$(\mu - \mu_1)/\mu$ for spherical (dots) and nonspherical (triangles) particle suspensions. Green triangles represent the results of Boyer *et al.*[11] Line represents the fit given by Eq. (15).

suspensions, for any constant μ_m value. Naturally, these deviations become apparent at I_v values where particle interactions become relevant, i.e., $I_v < 10^{-1}$. Results suggests that the macroscopic friction coefficient of nonspherical particle suspensions plateaus to μ_1 at higher viscous numbers in comparison to the spherical particle suspensions. Also, at vanishing viscous numbers, the macroscopic friction coefficient of the nonspherical particle suspensions saturates to a higher μ_1 in comparison with spherical particle suspensions, for a given μ_m value. This agrees with measurements of the macroscopic friction coefficient for cornstarch suspensions close to jamming,[6] where $\mu_1 \approx 0.62$ in the experimental systems and $\mu_1 \approx 0.6$ in the simulations. In Sec. III G, it was concluded that the jamming volume fraction determines the minimum value of the macroscopic friction coefficient. Considering that the nonspherical suspension simulated here jams around $\phi_J^{non-spherical} = 0.53$, which is lower than the jamming volume fraction for spherical particles ($\phi_J^{spherical} = 0.576$) at the same μ_m value ($\mu_m = 1$), the larger μ_1 observed here can be rationalized.

It is intriguing to see whether one can generalize these variations in μ with particle shapes and microscopic friction coefficients to arrive at a common curve for all available data. By (a) normalizing I_v with $I_v^{2\mu_1}$ [where $I_v^{2\mu_1} = I_v(\mu = 2\mu_1)$] to account for the shift in I_v values at which μ plateaus to μ_1 and (b) setting upper and lower bounds to the variation in μ by using $(\mu - \mu_1)/\mu$ as the measure of the variation of μ with I_v, the results collapses nicely to a single curve, for both spherical and nonspherical particle suspensions, across varying μ_m values [see Fig. 11(b)]. The results of Boyer *et al.*[11] are shown for comparison and also agrees with the curve. This common relationship can be fitted using the empirical expression

$$\frac{\mu - \mu_1}{\mu} = \frac{\sqrt{I_v}}{\sqrt{I_v} + \sqrt{I_v^{2\mu_1}}}, \tag{15}$$

which in turn gives:

$$\mu = \mu_1\left(1 + \sqrt{\frac{I_v}{I_v^{2\mu_1}}}\right). \tag{16}$$

The terms ϕ_m, μ_1, I_0 from Eq. (4) are incorporated in $I_v^{2\mu_1}$ in Eq. (16). Since I_0 and μ_2 do not change significantly with μ_m, $I_v^{2\mu_1}$ becomes a function of the free parameter ϕ_m. Even though the simulation results reasonably conform to the expression given by Eq. (15), it should be mentioned that the validity of the expression at high viscous numbers ($I_v > 0.5$) is suspect, as we have no experimental data in this regime. Experimental data for nonspherical particles at viscous numbers high enough to obtain $I_v^{2\mu_1}$ are also absent, which prevents us from further validation.

IV. CONCLUSION

We analyze the behavior of the macroscopic friction coefficient (μ) under different microscopic friction coefficients (μ_m) using 3D numerical simulations. The predictions of μ from simulations agree with earlier predictions of viscous number granular suspension rheology. We find that when $\mu_m > 0.3$, the viscous number rheology is largely insensitive to the value of μ_m. By changing the jamming volume fraction ϕ_m with the changes in shear stresses and μ_m, we analyze μ in terms of distance to jamming ($\phi_m - \phi$) and provide phenomenological but analytic formulas that match the observations. Our results also suggest that the behavior of μ across various μ_m and viscous numbers (I_v) can be reduced to effects of the distance to jamming. The study of changes in the average coordination number (Z) with the viscous number (I_v) shows that Z smoothly decreases from Z_J (Z at jamming) to zero with increasing viscous number, where Z_J is again determined by μ_m. Our results suggest that the minimum μ achieved is inversely related to the jamming volume fraction and Z_J. Finally, we show that with appropriate scaling, a common curve for the variation of μ with I_v emerges for both spherical and nonspherical particles under varying μ_m values.

ACKNOWLEDGMENTS

We would like to thank SURFsara for using their HPC infrastructure and for providing support (Project No. 00231267). Author V.S. acknowledges funding by NWO, Netherlands under the CSER program (Project No. 14CSER026).

There are no conflicts of interests.

REFERENCES

[1] Y. S. Lee, E. D. Wetzel, and N. J. Wagner, "The ballistic impact characteristics of Kevlar® woven fabrics impregnated with a colloidal shear thickening fluid," J. Mater. Sci. **38**, 2825–2833 (2003).

[2] M. Li, B. Lyu, J. Yuan, C. Dong, and W. Dai, "Shear-thickening polishing method," Int. J. Mach. Tools Manuf. **94**, 88–99 (2015).

[3]M. Decker, C. Halbach, C. Nam, N. Wagner, and E. Wetzel, "Stab resistance of shear thickening fluid (STF)-treated fabrics," Compos. Sci. Technol. **67**, 565–578 (2007).
[4]C. D. Cwalina, C. M. McCutcheon, R. D. Dombrowski, and N. J. Wagner, "Engineering enhanced cut and puncture resistance into the thermal micrometeoroid garment (TMG) using shear thickening fluid (STF)–Armor^{TM} absorber layers," Compos. Sci. Technol. **131**, 61–66 (2016).
[5]M. M. Denn, J. F. Morris, and D. Bonn, "Shear thickening in concentrated suspensions of smooth spheres in Newtonian suspending fluids," Soft matter **14**, 170–184 (2018).
[6]A. Fall, F. Bertrand, G. Ovarlez, and D. Bonn, "Shear thickening of cornstarch suspensions," J. Rheol. **56**, 575–591 (2012).
[7]A. Fall, F. Bertrand, D. Hautemayou, C. Mézière, P. Moucheront, A. Lemaitre, and G. Ovarlez, "Macroscopic discontinuous shear thickening versus local shear jamming in cornstarch," Phys. Rev. Lett. **114**, 098301 (2015).
[8]E. Brown and H. M. Jaeger, "Shear thickening in concentrated suspensions: Phenomenology, mechanisms and relations to jamming," Rep. Prog. Phys. **77**, 046602 (2014).
[9]M. M. Denn and J. F. Morris, "Rheology of non-Brownian suspensions," Annu. Rev. Chem. Biomol. Eng. **5**, 203–228 (2014).
[10]C. D. Cwalina and N. J. Wagner, "Material properties of the shear-thickened state in concentrated near hard-sphere colloidal dispersions," J. Rheol. **58**, 949–967 (2014).
[11]F. Boyer, É. Guazzelli, and O. Pouliquen, "Unifying suspension and granular rheology," Phys. Rev. Lett. **107**, 188301 (2011).
[12]R. Mari, R. Seto, J. F. Morris, and M. M. Denn, "Shear thickening, frictionless and frictional rheologies in non-brownian suspensions," J. Rheol. **58**, 1693–1724 (2014).
[13]R. Seto, R. Mari, J. F. Morris, and M. M. Denn, "Discontinuous shear thickening of frictional hard-sphere suspensions," Phys. Rev. Lett. **111**, 218301 (2013).
[14]C. Ness and J. Sun, "Shear thickening regimes of dense non-Brownian suspensions," Soft Matter **12**, 914–924 (2015).
[15]J. Comtet, G. Chatté, A. Niguès, L. Bocquet, A. Siria, and A. Colin, "Pairwise frictional profile between particles determines discontinuous shear thickening transition in non-colloidal suspensions," Nat. Commun. **8**, 15633 (2017).
[16]N. Y. C. Lin, B. M. Guy, M. Hermes, C. Ness, J. Sun, W. C. K. Poon, and I. Cohen, "Hydrodynamic and contact contributions to continuous shear thickening in colloidal suspensions," Phys. Rev. Lett. **115**, 228304 (2015).
[17]Z. Pan, H. de Cagny, B. Weber, and D. Bonn, "S-shaped flow curves of shear thickening suspensions: Direct observation of frictional rheology," Phys. Rev. E **92**, 032202 (2015).
[18]J. R. Royer, D. L. Blair, and S. D. Hudson, "Rheological signature of frictional interactions in shear thickening suspensions," Phys. Rev. Lett. **116**, 188301 (2016).
[19]N. Huang, G. Ovarlez, F. Bertrand, S. Rodts, P. Coussot, and D. Bonn, "Flow of wet granular materials," Phys. Rev. Lett. **94**, 028301 (2005).
[20]S. Gallier, E. Lemaire, F. Peters, and L. Lobry, "Rheology of sheared suspensions of rough frictional particles," J. Fluid Mech. **757**, 514–549 (2014).
[21]W. Chèvremont, B. Chareyre, and H. Bodiguel, "Quantitative study of the rheology of frictional suspensions: Influence of friction coefficient in a large range of viscous numbers," Phys. Rev. Fluids **4**, 064302 (2019).
[22]M. Trulsson, E. DeGiuli, and M. Wyart, "Effect of friction on dense suspension flows of hard particles," Phys. Rev. E **95**, 012605 (2017).
[23]A. Singh, R. Mari, M. M. Denn, and J. F. Morris, "A constitutive model for simple shear of dense frictional suspensions," J. Rheol. **62**, 457–468 (2018).
[24]M. Wyart and M. E. Cates, "Discontinuous shear thickening without inertia in dense non-Brownian suspensions," Phys. Rev. Lett. **112**, 098302 (2014).
[25]E. Lorenz, V. Sivadasan, D. Bonn, and A. G. Hoekstra, "Combined lattice-Boltzmann and rigid-body method for simulations of shear-thickening dense suspensions of hard particles," Comput. Fluids **172**, 474 (2018).
[26]D. Noble and J. Torczynski, "A lattice-Boltzmann method for partially saturated computational cells," Int. J. Mod. Phys. C **9**, 1189–1201 (1998).
[27]S. Luding, "Cohesive, frictional powders: Contact models for tension," Granular Matter **10**, 235–246 (2008).
[28]S. H. Maron and P. E. Pierce, "Application of Ree-Eyring generalized flow theory to suspensions of spherical particles," J. Colloid Sci. **11**, 80–95 (1956).
[29]I. M. Krieger and T. J. Dougherty, "A mechanism for non-Newtonian flow in suspensions of rigid spheres," Trans. Soc. Rheol. **3**, 137–152 (1959).
[30]I. E. Zarraga, D. A. Hill, and D. T. Leighton, Jr., "The characterization of the total stress of concentrated suspensions of noncolloidal spheres in Newtonian fluids," J. Rheol. **44**, 185–220 (2000).
[31]G. Ovarlez, F. Bertrand, and S. Rodts, "Local determination of the constitutive law of a dense suspension of noncolloidal particles through magnetic resonance imaging," J. Rheol. **50**, 259–292 (2006).
[32]Z. Pan, H. de Cagny, M. Habibi, and D. Bonn, "Normal stresses in shear thickening granular suspensions," Soft Matter **13**, 3734–3740 (2017).
[33]S.-C. Dai, E. Bertevas, F. Qi, and R. I. Tanner, "Viscometric functions for non-colloidal sphere suspensions with Newtonian matrices," J. Rheol. **57**, 493–510 (2013).
[34]A. Singh and P. R. Nott, "Experimental measurements of the normal stresses in sheared stokesian suspensions," J. Fluid Mech. **490**, 293–320 (2003).
[35]É. Couturier, F. Boyer, O. Pouliquen, and É. Guazzelli, "Suspensions in a tilted trough: Second normal stress difference," J. Fluid Mech. **686**, 26–39 (2011).
[36]T. Dbouk, L. Lobry, and E. Lemaire, "Normal stresses in concentrated non-Brownian suspensions," J. Fluid Mech. **715**, 239–272 (2013).
[37]A. Sierou and J. Brady, "Rheology and microstructure in concentrated noncolloidal suspensions," J. Rheol. **46**, 1031–1056 (2002).
[38]S. Gallier, E. Lemaire, L. Lobry, and F. Peters, "Effect of confinement in wall-bounded non-colloidal suspensions," J. Fluid Mech. **799**, 100–127 (2016).
[39]R. Seto and G. G. Giusteri, "Normal stress differences in dense suspensions," J. Fluid Mech. **857**, 200–215 (2018).
[40]C. Cassar, M. Nicolas, and O. Pouliquen, "Submarine granular flows down inclined planes," Phys. fluids **17**, 103301 (2005).
[41]P. Jop, "Rheological properties of dense granular flows," C. R. Phys. **16**, 62–72 (2015).
[42]J. E. Thomas, K. Ramola, A. Singh, R. Mari, J. F. Morris, and B. Chakraborty, "Microscopic origin of frictional rheology in dense suspensions: Correlations in force space," Phys. Rev. Lett. **121**, 128002 (2018).
[43]R. Mari, R. Seto, J. F. Morris, and M. M. Denn, "Nonmonotonic flow curves of shear thickening suspensions," Phys. Rev. E **91**, 052302 (2015).
[44]J. Y. Moon, S. Dai, L. Chang, J. S. Lee, and R. I. Tanner, "The effect of sphere roughness on the rheology of concentrated suspensions," J. Non-Newtonian Fluid Mech. **223**, 233–239 (2015).
[45]D. Lootens, H. Van Damme, Y. Hémar, and P. Hébraud, "Dilatant flow of concentrated suspensions of rough particles," Phys. Rev. Lett. **95**, 268302 (2005).
[46]C.-P. Hsu, S. N. Ramakrishna, M. Zanini, N. D. Spencer, and L. Isa, "Roughness-dependent tribology effects on discontinuous shear thickening," Proc. Natl. Acad. Sci. U. S. A. **115**, 5117–5122 (2018).
[47]F. Da Cruz, S. Emam, M. Prochnow, J.-N. Roux, and F. Chevoir, "Rheophysics of dense granular materials: Discrete simulation of plane shear flows," Phys. Rev. E **72**, 021309 (2005).
[48]A. Singh, J. F. Morris, and M. M. Denn, "Microstructural description of shear-thickening suspensions," EPJ Web Conf. **140**, 09023 (2017).
[49]C. Song, P. Wang, and H. A. Makse, "A phase diagram for jammed matter," Nature **453**, 629 (2008).